IEEE Access
Multidisciplinary | Rapid Review | Open Access Journal

Received June 17, 2021, accepted June 24, 2021, date of publication June 29, 2021, date of current version July 8, 2021.

Digital Object Identifier 10.1109/ACCESS.2021.3093359

Quantitative Analysis of Back-EMF of a Dual-Permanent-Magnet-Excited Machine: Alert to Flux Density Harmonics Which Make a Negative Contribution to Back-EMF

YUJUN SHI[1], (Member, IEEE), JUNWEN ZHONG[1], AND LINNI JIAN[2], (Senior Member, IEEE)

[1]Department of Electromechanical Engineering, University of Macau, Macao 999078, China
[2]University Key Laboratory of Advanced Wireless Communications of Guangdong Province, Department of Electrical and Electronic Engineering, Southern University of Science and Technology, Shenzhen 518055, China

Corresponding author: Linni Jian (jianln@sustech.edu.cn)

This work was supported in part by the Department of Education of Guangdong Province under Project 2020ZDZX3002, and in part by the Science and Technology Innovation Committee of Shenzhen under Project 20200925154042003.

ABSTRACT Recently, the dual-permanent-magnet-excited (DPME) machine has attracted growing attention due to its high torque density. Due to the bidirectional field modulated effect (BFME), airgap flux density harmonics (AFDHs) are more complex and abundant than traditional permanent magnet synchronous machines (PMSMs). Moreover, the back-electromotive force (EMF) generated by AFDHs is also complex. Unfortunately, only a few papers qualitatively analyze back-EMF. The qualitative analysis for back-EMF can reveal some important conclusions; for example, only AFDHs meeting specific pole pair numbers (PPNs) can generate back-EMF. However, it may also ignore some details and valuable findings. In this paper, a purely analytical magnetomotive force (MMF) permeance model (PAMPM) for a DPME machine is built to quantitatively analyze the back-EMF. The PAMPM does not require a numerical method, such as conformal transformation. With the PAMPM, AFDHs that contribute to the generation of back-EMF can be recognized and quantified. Interestingly, AFDHs with $m_2p_2 = np_3$ cause PM flux-linkage to have a dc bias, and not all AFDHs play a positive role in the generation of back-EMF. The main recognition results are as follows: 1) the S-II and R-II types of AFDHs in a 12/10 DPME machine overall make a negative contribution to the generation of back-EMF; and 2) AFDHs with PPN=22 in the two types mainly cause a negative contribution. To further verify the above results, 2D finite element simulation and experimental tests of a prototype machine are also conducted.

INDEX TERMS Back-EMF, field modulated, PM machine, vernier machine, analytical method.

NOMENCLATURE

p_1	PPN of rotor PMs/number of rotor slots
p_2	PPN of stator PMs/number of stator slots
m, y_1, p_3	Phase number, coil pitch, PPN of armature windings
L_e, g	Axial effective length, length of airgap. Unit: mm
B_r	Remanence of PMs. Unit: T
u_r	Relative permeability of PMs
u_0	Permeability in vacuum
K_s	Opening ratio of stator slot width to stator slot pitch
K_r	Opening ratio of rotor slot width to rotor slot pitch
α_s, α_r	One stator slot pitch, one rotor slot pitch. Unit: rad
n_c	Turn number of each coil
N_p	Turn number in series per phase
R_{so}	Outer radius of stator iron. Unit: mm
R_{si}	Inner radius of stator iron. Unit: mm
R_{ro}	Outer radius of rotor iron. Unit: mm
R_{ri}	Inner radius of rotor iron. Unit: mm
h_s, h_{sm}	Depth of stator slots, thickness of stator PMs. Unit: mm

The associate editor coordinating the review of this manuscript and approving it for publication was R. K. Saket.

h_{rm}, r_g	Depth of rotor slots, average radius of airgap. Unit: mm
θ_0	Initial position of rotor. Unit: rad
θ_{m}	Airgap between a rotor PM and its adjacent rotor tooth. Unit: rad
n_r	Mechanical rotational speed of rotor. Unit: r/min
Ω_r	Mechanical rotational speed of rotor. Unit: rad/s
$F^R_{\mathrm{PM}}(\theta_s, t)$	Airgap MMF produced by rotor PMs. Unit: A
m_1	Harmonic order of airgap MMF produced by rotor PMs
F_{m1}	m_1-*th* harmonic coefficient of airgap MMF produced by rotor PMs. Unit: A
F_r,$-F_{r1}$	Maximum and minimum value of waveform of rotor PM MMF. Unit: A
$F^S_{\mathrm{PM}}(\theta_s)$	Airgap MMF generated by stator PMs. Unit: A
m_2	Harmonic order of airgap MMF produced by stator PMs
F_{m2}	m_2-*th* harmonic coefficient of airgap MMF produced by stator PMs. Unit: A
F_s, $-F_{s1}$	Maximum and minimum value of waveform of stator PM MMF. Unit: A
k_1	Harmonic order of airgap permeance due to the slotted stator
k_2	Harmonic order of airgap permeance due to the slotted rotor
n	Harmonic order of winding function
v	Harmonic order of back-EMF
f_v	Harmonic frequency of back-EMF. Unit: Hz
E_v	Amplitude of harmonic back-EMF. Unit: V

I. INTRODUCTION

Benefiting from the ''magnetic gearing effect'', permanent-magnet vernier machines (PMVMs) have the inherent advantage of high torque density and can directly drive the load without the help of intermediate transmission devices such as mechanical gearboxes, thus making PMVMs outstanding candidates for direct drive applications [1]–[6]. To date, various topologies have been proposed for PMVMs with high performance. According to the location of permanent magnets (PMs), PMVMs can be generally divided into three types [7]–[9]: 1) stator type (ST) [10], [11]; 2) rotor type (RT) [12], [13] and 3) stator and rotor type (SRT) [14], [15]. Here, the ST or RT PMVM signifies that only the stator or the rotor has PMs, while the SRT PMVM, also called the dual-permanent-magnet-excited (DPME) machine [7]–[9], [16], means that both the stator and rotor have PMs.

From the perspective of magnetic load, DPME machines with PMs on both stators and rotors have the significant advantage of higher torque density over the other two types, which has been proven in [16]–[18]. Thus, DPME machines have attracted growing attention recently. In fact, the DPME machine was first proposed in 1995 and analyzed by using the finite element method (FEM) combined with mathematical derivation [19]. The structural characteristics are 1) both stator and rotor PMs adopt the same polarity (see Fig. 1) and 2) stator slots for installing stator PMs are the same as those for accommodating armature windings (see Fig. 1). However, since field modulation theory (FMT) did not appear at that time, the DPME machine attracted little attention. With the emergence of FMT in 1999 [20], DPME machines following the other two types of PMVMs have been developing rapidly. In [16], a new DPME machine was presented with a more flexible slot-pole design since slots for installing stator PMs could be different from those for accommodating armature windings. Moreover, the bidirectional field modulated effect (BFME) was proposed to explain the working principle. In [21], an equivalent magnetic network (EMN) model combining the adaptive mesh method was proposed for a DPME machine to reduce the time consumption of the FEM and ensure the accuracy of the EMN. In [17] and [22], DPME machines with Halbach PM arrays were presented to improve torque density. In [7], a new DPME machine with nonuniformly distributed stator PMs was proposed to further improve the torque capability. Due to the nonuniformly distributed stator PMs, multiple field harmonics can be effectively used to produce torque. In [20], a new DPME machine with stator PMs mounted on stator tooth tips was proposed to improve the torque density and power factor. In [23], a DPME machine with split stator teeth and Halbach PM arrays was proposed and compared with other types of PMVMs. These results indicate that the proposed machine can significantly increase the back-electromotive force (EMF) and torque. In [24], Wang *et al.* proposed a hybrid-excited DPME machine with two sets of windings to enhance torque capability and expand the constant power speed range. As reported in [25], the DPME machine in [24] was designed as a wind power generator, an analytical model was built, and both constant voltage control and maximum power point tracking (MPPT) control were achieved. For the same purpose in [24], Wang *et al.* proposed a new hybrid-excited DPME machine with one set of windings in [26]. The remarkable characteristic of the machine is that windings are injected into the ac current with a dc bias. In [18], torque component quantification of a DPME machine was conducted to identify the torque contribution of stator PMs and rotor PMs. It is shown that the torque contribution of rotor PMs is much larger than that of stator PMs, so rotor PMs should be designed with higher priority. In [27], surface response methodology was used to optimize a DPME machine for increasing torque and decreasing PM usage. In [28], the performance between DPME machines with fewer stator poles and fewer rotor poles was compared, and FEM results confirmed that the DPME machine with fewer rotor poles had a better electromagnetic performance. In [9], four DPME machines with the same rotor structure but different stator structures were comparatively studied

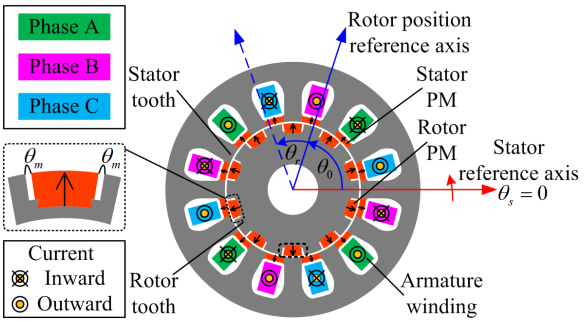

FIGURE 1. Configuration of p_2/p_1 DPME machine.

and optimized by using an improved Tabu search coupled with FEM. In [29], the control of a DPME machine was realized by space vector pulse width modulation.

According to the above literature review, the research on DPME machines mainly focuses on new topologies [6], [7], [16], [17], [19], [20], [22]–[26], design and optimization [8], [14], [15], [18], [21], [27], performance comparison [9], [28], [30], [31] and control [25], [29].

Back-EMF is a key physical quantity in electrical machines (EMs), which designers always concern [32]. For the DPME machine (see Fig. 1), both the stator and rotor adopt teeth-slot structures; both the stator and rotor have PMs, and the PPN of stator PMs is unequal to that of rotor PMs. Due to the two tooth-slot structures, the magnetic field generated by stator PMs is modulated into abundant airgap flux density harmonics (AFDHs) through rotor teeth, while the magnetic field generated by rotor PMs is modulated into numerous AFDHs through stator teeth. Compared with traditional PMSMs, the AFDHs of DPME machines are more abundant and complex. Regarding the generation of back-EMF in a DPME machine, two questions (Qs) naturally occur. Q1: Which AFDHs contribute to the generation of back-EMF? Q2: Do AFDHs that produce back-EMF all play a positive role in the generation of back-EMF? If not, which AFDHs will make a negative contribution to the generation of back-EMF? As per the previous literature review, only [7], [22], and [25] involve the expression of back-EMF, but only [7] and [25] answer Q1 clearly, which indicates that AFDHs meeting only the specific PPN relationship can generate back-EMF. However, [7] and [25] cannot answer Q2 due to the qualitative expression of back-EMF. Unfortunately, work to solve Q2 is still lacking. Therefore, it is necessary to quantitatively analyze the back-EMF of the DPME machine and recognize and quantify AFDHs that contribute to the generation of back-EMF. This can help EM designers recognize these AFDHs, which make a negative contribution to the generation of back-EMF at the beginning of EM design, and then optimize the DPME machine better.

To quantitatively analyze the back-EMF of the DPME machine and recognize and quantify the AFDHs that generate back-EMF, the key is to obtain the expression of the modulated airgap flux density (AFD). Generally, there are two methods to calculate the modulated AFD [33]: one is to adopt the airgap permeance model [34]–[39], and the other is to solve mathematical equations in different subdomains [40]–[45], such as Laplace/quasi-Poissonian equations or Maxwell's equations. For the former method, a numerical method such as conformal transformation is usually used to calculate the harmonic coefficient in the airgap permeance function. Undeniably, the two methods are accurate and effective, but the derivation is complex, and many quantities are not intuitive.

To solve the mentioned Q2, the back-EMF of the DPME machine is quantitatively analyzed based on a purely analytical magnetomotive force (MMF) permeance model (PAMPM) in this paper. The novelty of this paper is that 1) a PAMPM is established for the DPME machine, and the PAMPM does not require any numerical method, such as the complicated conformal transformation or solving mathematical equations in different subdomains; 2) the general expressions of AFD, PM flux-linkage (PMFL), and back-EMF are derived based on the PAMPM, which can be used for quantitative analysis and calculations without the help of FEM; 3) the PAMPM and derived expressions are associated with the dimensional parameters, thereby enabling the analysis of the influence of the dimensional parameters on the performance of the DPME machine.

The main contributions of this paper are as follows:

1) Recognizing and quantifying the AFDHs that make a negative contribution to the generation of back-EMF. This can help EM designers optimize DPME machines in a targeted manner.
2) Defining the contribution rate to evaluate the contribution of different types of AFDHs to back-EMF.
3) Discovering that the AFDHs with $m_2p_2 = np_3$ cause PM flux-linkage to have a dc bias.

II. PURELY ANALYTICAL MMF PERMEANCE MODEL

Before building a PAMPM for the DPME machine, reference axes and angles need to be defined, as illustrated in Fig. 1. Moreover, the following assumptions need to be made:

1) The permeability of stator iron and rotor iron is infinite, so the magnetic saturation is neglected.
2) The stator and rotor slots are infinitely deep when deriving airgap permeance.
3) The fringing and end effects are ignored.
4) Only the radial flux density is considered.
5) Waveforms of airgap PM MMF are square waves.

A. MMF MODEL

As shown in Fig. 2(b), one can obtain the waveform of the airgap rotor PM MMF without modulation by the stator teeth according to the stator reference axis in Fig. 2(a) and the 5th assumption.

Thus, the expression of airgap rotor PM MMF, $F^R_{\mathrm{PM}}(\theta_s, t)$, can be expressed by Fourier series expansion, i.e.,

$$F^R_{\mathrm{PM}}(\theta_s, t) = \sum_{m_1=1}^{\infty} F_{m_1} \cos\left[m_1 p_1 \left(\theta_s - \Omega_r t - \theta_0\right)\right] \quad (1)$$

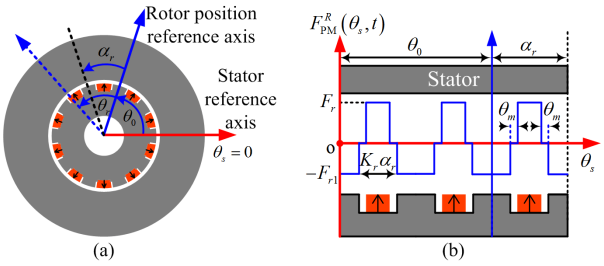

FIGURE 2. Derivation of airgap rotor PM MMF. (a) Model to obtain airgap rotor PM MMF. (b) Waveform of airgap rotor PM MMF ($t = 0$).

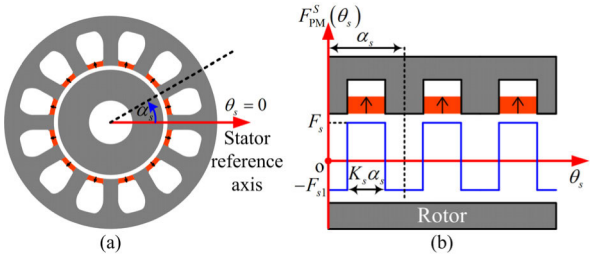

FIGURE 3. Derivation of airgap stator PM MMF. (a) Model to obtain airgap stator PM MMF. (b) Waveform of airgap stator PM MMF.

where F_{m_1} can be obtained by

Methods for calculating F_r and F_{r1} in (2), as shown at the bottom of the page are presented in Appendix-A.

As shown in Fig. 3(b), one can also obtain the waveform of the airgap stator PM MMF without modulation by the rotor teeth based on the stator reference axis in Fig. 3(a) and the 5$^{\text{th}}$ assumption.

Thus, the expression of the airgap stator PM MMF, $F^S_{\text{PM}}(\theta_s)$, can be expressed by Fourier series expansion, i.e.,

$$\begin{cases} F^S_{\text{PM}}(\theta_s) = \sum_{m_2=1}^{\infty} F_{m_2} \cos(m_2 p_2 \theta_s) \\ F_{m_2} = \dfrac{2(F_s + F_{s1}) \sin[m_2\pi(K_s - 1)]}{m_2\pi} \end{cases} \tag{3}$$

Methods for calculating F_s and F_{s1} in (3) are given in Appendix-B. Note that the effect of the slotted stator on the airgap stator PM MMF is considered in (3). In the derivation of F_s and F_{s1}, the reluctance of the flux lines starting from a stator PM and passing through a stator slot has been taken into account (see Appendix-B).

B. PERMEANCE MODEL

Fig. 4 shows the derivation model of airgap permeance due to the slotted stator. According to the definition of permeance, the airgap permeance due to a slotted stator, i.e., $\lambda_s(\theta_s)$, can

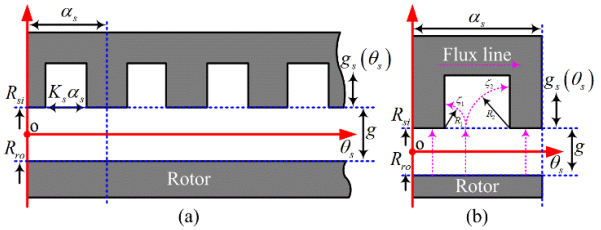

FIGURE 4. Derivation of airgap permeance due to slotted stator. (a) Calculation model based on stator reference axis. (b) Flux line paths in one stator slot pitch.

be expressed as

$$\lambda_s(\theta_s) = \mu_0 / [g + g_s(\theta_s)] \tag{4}$$

where $g_s(\theta_s)$ indicates the length of the additional airgap due to the slotted stator. When stator iron is not slotted, $g_s(\theta_s)$ is equal to zero.

Fig. 4(b) describes flux lines going through the stator in one stator slot pitch based on assumptions 1-4. Additionally, it is assumed that the flux lines enter the stator teeth from a stator slot along quarter circles with radii R_1 and R_2. In Fig. 4(b), R_1 and R_2 can be obtained by the expression below:

$$R_1 = 2R_{si} \sin\left(\frac{\theta_s}{2} - \frac{\alpha_s - K_s\alpha_s}{4}\right) \tag{5}$$

$$R_2 = 2R_{si} \sin\left(\frac{\alpha_s + K_s\alpha_s}{4} - \frac{\theta_s}{2}\right) \tag{6}$$

Therefore, the corresponding arc lengths ζ_1 and ζ_2 [46] can be obtained as

$$\begin{cases} \zeta_1 = \dfrac{\pi}{2} R_1 = \pi R_{si} \sin\left(\dfrac{\theta_s}{2} - \dfrac{\alpha_s - K_s\alpha_s}{4}\right) \\ \zeta_2 = \dfrac{\pi}{2} R_2 = \pi R_{si} \sin\left(\dfrac{\alpha_s + K_s\alpha_s}{4} - \dfrac{\theta_s}{2}\right) \end{cases} \tag{7}$$

On the other hand, $g_s(\theta_s)$ can be regarded as the equivalent length of ζ_1 and ζ_2 in parallel [33], which can be expressed as

$$g_s(\theta_s) = \frac{\zeta_1\zeta_2}{\zeta_1 + \zeta_2}, \quad \theta_s \in \left[\frac{\alpha_s - K_s\alpha_s}{2}, \frac{\alpha_s + K_s\alpha_s}{2}\right] \tag{8}$$

Substituting (7) and (8) into (4) first and then expanding (4) into a Fourier series, one can obtain the airgap permeance due to the slotted stator as follows:

$$\lambda_s(\theta_s) = \lambda_s^0 + \sum_{k_1=1}^{\infty} \lambda_s^{k_1} \cos(k_1 p_2 \theta_s) \tag{9}$$

where λ_s^0 and $\lambda_s^{k_1}$ are coefficients of the dc component and the k_1-*th* harmonic of $\lambda_s(\theta_s)$, respectively.

Fig. 5 shows the waveform of (4) in one stator pitch. It is very complex to calculate λ_s^0 and $\lambda_s^{k_1}$ directly according to (4). To calculate λ_s^0 and $\lambda_s^{k_1}$ conveniently, the curve in Fig. 5 can be

$$F_{m_1} = \frac{2F_r \sin[m_1\pi(K_r - 1) - m_1 p_1 \theta_m] + 2F_{r1} \sin[m_1\pi(K_r - 1)]}{m_1\pi} \tag{2}$$

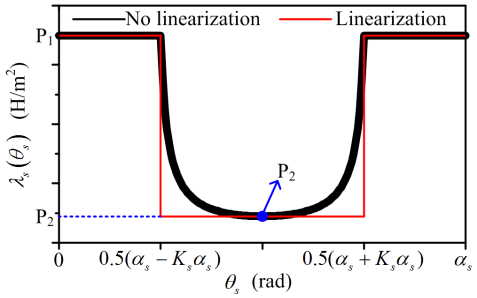

FIGURE 5. Waveform of (4) in one stator pitch.

simplified by linearization. After linearization, the waveform turns into a square wave. Based on the Fourier series expansion of the square wave, λ_s^0 and $\lambda_s^{k_1}$ can be calculated by

$$\begin{cases} \mathrm{P}_1 = \dfrac{\mu_0}{g}, \mathrm{P}_2 = \dfrac{2\mu_0}{2g + \pi R_{si} \sin\left(K_s\alpha_s/4\right)} \\ \lambda_s^0 = \mathrm{P}_2 K_s + \mathrm{P}_1 \left(1 - K_s\right) \\ \lambda_s^{k_1} = \dfrac{2\left(\mathrm{P}_1 - \mathrm{P}_2\right) \sin\left[k_1\pi \left(1 - K_s\right)\right]}{k_1\pi} \end{cases} \tag{10}$$

Similar to the derivation of $\lambda_s(\theta_s)$, the airgap permeance due to the slotted rotor, i.e., $\lambda_r(\theta_s, t)$, can be expressed as

$$\lambda_r(\theta_s, t) = \lambda_r^0 + \sum_{k_2=1}^{\infty} \lambda_r^{k_2} \cos\left[k_2 p_1 \left(\theta_s - \Omega_r t - \theta_0\right)\right] \tag{11}$$

where λ_r^0 and $\lambda_r^{k_2}$ are coefficients of the dc component and the k_2-*th* harmonic of $\lambda_r(\theta_s, t)$. Likewise, λ_r^0 and $\lambda_r^{k_2}$ can be obtained after linearization, i.e.,

$$\begin{cases} \mathrm{P}_3 = \dfrac{\mu_0}{g}, \mathrm{P}_4 = \dfrac{2\mu_0}{2g + \pi R_{so} \sin\left(K_r\alpha_r/4\right)} \\ \lambda_r^0 = \mathrm{P}_4 K_r + \mathrm{P}_3 \left(1 - K_r\right) \\ \lambda_r^{k_2} = \dfrac{2\left(\mathrm{P}_3 - \mathrm{P}_4\right) \sin\left[k_2\pi \left(1 - K_r\right)\right]}{k_2\pi} \end{cases} \tag{12}$$

C. SIMULATION VERIFICATION

As shown in Fig. 1, a 3-phase 12/10 (p_2/p_1) DPME machine with linear iron is used to build 2D FEM models to verify the foregoing analysis. Note that all FEM models are built by JMAG-Designer software. The parameters illustrated in Fig. 6 are listed in Table 1.

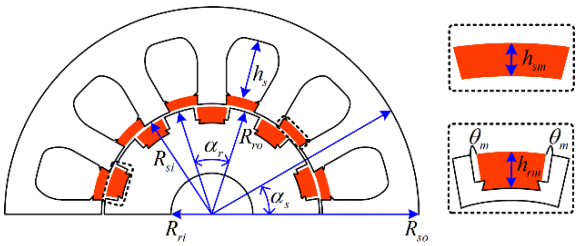

FIGURE 6. Dimensional parameter model.

Figs. 7 and 8 show the airgap rotor PM MMF and the airgap stator PM MMF, respectively. Clearly, the analytical and

TABLE 1. Specifications of 12/10 DPME machine.

m	3	h_s	25 mm	R_{ro}	39.4 mm	u_r	1.05
p_2/p_1	12/10	h_{sm}	3.5 mm	R_{ri}	15 mm	r_g	39.7 mm
p_3	2	K_s	0.5	h_{rm}	6 mm	g	0.6 mm
L_e	60 mm	α_s	$\pi/6$	K_r	0.5	θ_0	$2\pi/5$
R_{so}	75 mm	y_1	3	α_r	$\pi/5$	θ_m	1.45 $\pi/180$
R_{si}	40 mm	n_c	288	B_r	1.2 T	n_r	120 r/min

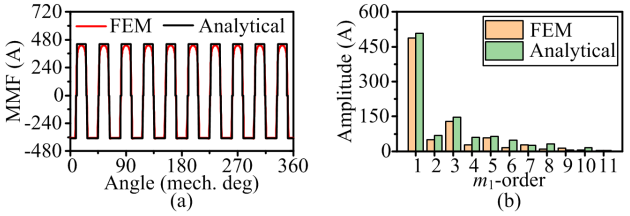

FIGURE 7. Airgap rotor PM MMF. (a) Waveforms. (b) Spectra.

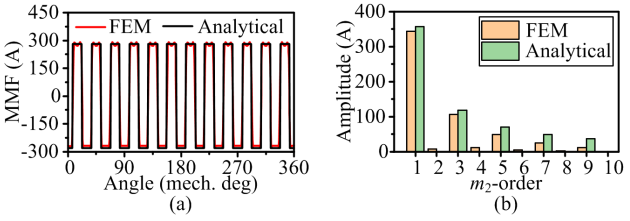

FIGURE 8. Airgap stator PM MMF. (a) Waveforms. (b) Spectra.

FEM results are basically consistent. Note that the waveforms in Fig. 7(a) obtained by the FEM and analytical method are unsymmetrical about the zero of the y-axis. This is because the airgap reluctance at a rotor PM is different from that at a rotor tooth when $K_r = 0.5$ and $\theta_m = 1.45\ \pi/180$, which is also explained in detail in Appendix-A. According to Fig. 7(b), both odd- and even-order harmonics exist in the airgap rotor PM MMF, which agrees with (1) when $K_r = 0.5$ and $\theta_m = 1.45\ \pi/180$. As shown in Fig. 8(a), the waveforms of the stator PM MMF are symmetrical about the zero of the y-axis. This is because the airgap reluctance at a stator PM is equal to that at a stator tooth when $K_s = 0.5$, which is also explained in detail in Appendix-B. From Fig. 8(b), one can find that there are only odd-order harmonics in the airgap stator PM MMF, which coincides with (2) when $K_s = 0.5$. This is because F_{m_2} equals zero when $K_s = 0.5$ and m_2 is even.

To verify the airgap permeance models that are not linearized, the waveforms of airgap permeance can be obtained by FEM using the method presented in Appendix-C. As shown in Figs. 9 and 10, the analytical results are largely consistent with the FEM results, and the amplitude errors of each order harmonic arising from the assumptions are acceptable.

III. DERIVATION AND ANALYSIS OF BACK-EMF

The general expression of back-EMF in the DPME machine can be derived by the PAMPM. Based on the PAMPM, the expression of the AFD produced by PMs can be obtained

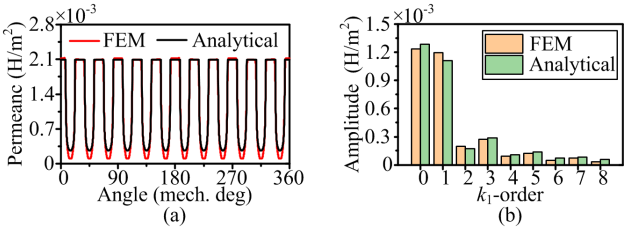

FIGURE 9. Airgap permeance due to the slotted stator. (a) Waveforms. (b) Spectra.

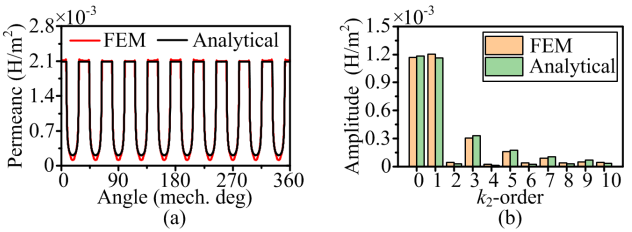

FIGURE 10. Airgap permeance due to the slotted rotor. (a) Waveforms. (b) Spectra.

first, followed by the PMFL and finally the back-EMF. Note that because of the BFME, one can calculate the AFD produced by stator PMs and the AFD produced by rotor PMs separately. By means of the general and purely analytical expressions of AFD and back-EMF, one can recognize and quantify the AFDHs that make a negative contribution to the generation of back-EMF.

A. AIRGAP FLUX DENSITY PRODUCED BY PMs

The AFD produced by stator PMs, i.e., $B^S_{\mathrm{PM}}(\theta_s, t)$, can be obtained by multiplying $F^S_{\mathrm{PM}}(\theta_s)$ and $\lambda_r(\theta_s, t)$, i.e.,

$$\begin{aligned} B^S_{\mathrm{PM}}(\theta_s, t) = &\sum_{m_2=1}^{\infty} \lambda_r^0 F_{m_2} \cos(m_2 p_2 \theta_s) \\ &+ \sum_{m_2=1}^{\infty}\sum_{k_2=1}^{\infty} \frac{\lambda_r^{k_2} F_{m_2}}{2} \cos[(m_2 p_2 \pm k_2 p_1)\theta_s \\ &\mp k_2 p_1 \Omega_r t \mp k_2 p_1 \theta_0] \end{aligned} \tag{13}$$

Similarly, the AFD produced by rotor PMs, i.e., $B^R_{\mathrm{PM}}(\theta_s, t)$, can be obtained by multiplying $F^R_{\mathrm{PM}}(\theta_s, t)$ and $\lambda_s(\theta_s)$, i.e.,

$$\begin{aligned} &B^R_{\mathrm{PM}}(\theta_s, t) \\ &= \sum_{m_1=1}^{\infty} \lambda_s^0 F_{m_1} \cos[m_1 p_1 \theta_s - (m_1 p_1 \Omega_r t + m_1 p_1 \theta_0)] \\ &\quad + \sum_{m_1=1}^{\infty}\sum_{k_1=1}^{\infty} \frac{\lambda_s^{k_1} F_{m_1}}{2} \cos[(m_1 p_1 \pm k_1 p_2)\theta_s \\ &\quad - (m_1 p_1 \Omega_r t + m_1 p_1 \theta_0)] \end{aligned} \tag{14}$$

From (13) and (14), one can see that the magnetic fields generated by stator and rotor PMs are modulated into abundant AFDHs. According to PPN, AFDHs can be divided into six types, in which the stator PMs and the rotor PMs produce three types. The six types of AFDHs are summarized in Table 2. From Table 2, one can find that:

1) The AFDH speed of S-I type is zero, i.e., this type of AFDHs is stationary.
2) Only the AFDH speed of the R-I type is synchronized with the rotor.
3) The AFDH speeds of the S-II, S-III, R-II, and R-III types are asynchronous with the rotor.

To verify (13) and (14), the 12/10 DPME machine with linear iron continues to be analyzed. Fig. 11 displays the AFDs produced by stator PMs and rotor PMs. As seen from Figs. 11(a) and 11(b), good agreement is nearly reached between the analytical and FEM results. Note that the FEM results for AFD in Fig. 11 (a) and 11 (b) are greater than the analytical results. This is mainly because in the derivation of airgap permeance, it is assumed that the flux lines enter iron teeth from a slot along quarter circles. As a result, the analytical results for the 1st-order permeance harmonics are smaller than those for the 1st-order permeance harmonics by FEM, as shown in Figs. 9(b) and 10(b). From Figs. 11(c) and 11(d), there are six types of AFDHs, which is consistent with the results inferred from Table 2.

TABLE 2. Airgap flux density harmonics produced by PMs.

Harmonic	Type	PPN	Speed	Amplitude
Produced by stator PMs	S-I	$m_2 p_2$	0	$\lambda_r^0 F_{m_2}$
	S-II	$m_2 p_2 + k_2 p_1$	$\frac{k_2 p_1 \Omega_r}{m_2 p_2 + k_2 p_1}$	$\frac{1}{2}\lambda_r^{k_2} F_{m_2}$
	S-III	$\lvert m_2 p_2 - k_2 p_1 \rvert$	$\frac{-k_2 p_1 \Omega_r}{m_2 p_2 - k_2 p_1}$	$\frac{1}{2}\lambda_r^{k_2} F_{m_2}$
Produced by rotor PMs	R-I	$m_1 p_1$	Ω_r	$\lambda_s^0 F_{m_1}$
	R-II	$m_1 p_1 + k_1 p_2$	$\frac{m_1 p_1 \Omega_r}{m_1 p_1 + k_1 p_2}$	$\frac{1}{2}\lambda_s^{k_1} F_{m_1}$
	R-III	$\lvert m_1 p_1 - k_1 p_2 \rvert$	$\frac{m_1 p_1 \Omega_r}{m_1 p_1 - k_1 p_2}$	$\frac{1}{2}\lambda_s^{k_1} F_{m_1}$

Moreover, Figs. 11(c) and 11(d) show that AFDH with the same PPN may be synthesized by different types of AFDHs. For instance, AFDHs with PPN = 10 in Fig. 11(d) are synthesized by R-I and R-III types of AFDHs. As shown in Table 3, the main components of the harmonic with PPN = 10 in Fig. 11(d), including type, amplitude, and phase angle, can be identified on the basis of the PAMPM. However, the FEM can only identify the amplitude and phase angle of the resultant harmonic.

B. PM FLUX-LINKAGE

The phase PMFL, i.e., $\varphi_{\mathrm{PM}}(t)$, can be calculated by

$$\begin{aligned} \varphi_{\mathrm{PM}}(t) &= \varphi^S_{\mathrm{PM}}(t) + \varphi^R_{\mathrm{PM}}(t) \\ &= r_g L_e \int_0^{2\pi} B^S_{\mathrm{PM}}(\theta_s, t) N(\theta_s) d\theta_s \\ &\quad + r_g L_e \int_0^{2\pi} B^R_{\mathrm{PM}}(\theta_s, t) N(\theta_s) d\theta_s \end{aligned} \tag{15}$$

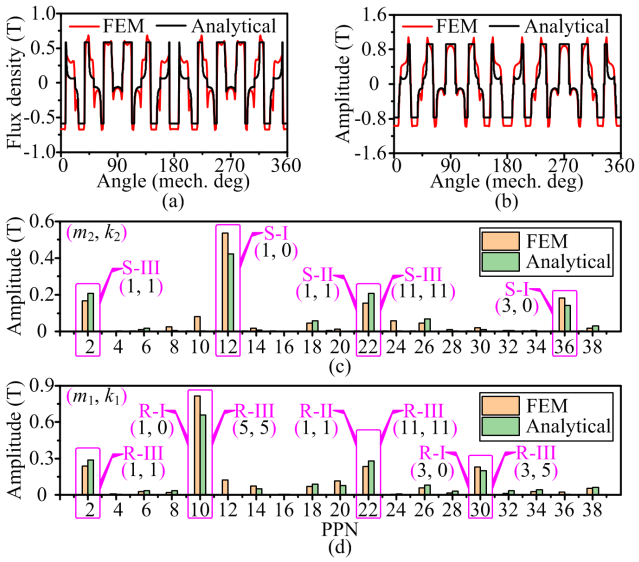

FIGURE 11. Airgap flux density and its spectrum. (a) Waveform of AFD produced by stator PMs. (b) Waveform of AFD produced by rotor PMs. (c) Spectra of Fig. 11(a). (d) Spectra of Fig. 11(b).

TABLE 3. Main components of harmonic with PPN = 10.

PPN	(m_1, k_1)	Type	Speed	Amplitude	Phase angle
10	(1, 0)	R-I	Ω_r	0.6 T	5π
	(5, 5)	R-III	$-5\Omega_r$	0.0075 T	-19π

where $N(\theta_s)$ refers to the winding function, which can be expressed as

$$\begin{cases} N(\theta_s) = \sum_{n=1}^{\infty} -\dfrac{2N_p k_{pn} k_{dn}}{n\pi p_3} \cos(np_3\theta_s) \\ k_{pn} = \sin\left(\dfrac{np_3\pi y_1}{p_2}\right), k_{dn} = \dfrac{6p_3 \sin(n\pi/6)}{p_2 \sin(n\pi p_3/p_2)} \end{cases} \tag{16}$$

where k_{pn} and k_{dn} are the coil-pitch factor of the *n-th* harmonic and the coil-distribution factor of the *n-th* harmonic, respectively. From (16), one can find that the harmonic order of the winding function has to do with p_2, p_3, and y_1. For example, when the winding is connected by full-pitch coils, k_{pn} is equal to $\sin(0.5n)$; when n is even, k_{pn} is equal to zero; therefore, there are only odd-order harmonics in the winding function.

Substituting (13), (14), and (16) into (15), one can obtain the general expression of the phase PMFL. Thus, the phase PMFLs produced by stator PMs and rotor PMs individually can be calculated by the following two expressions, i.e.,

$$\varphi_{\mathrm{PM}}^{S}(t) = \sum_{m_2=1}^{\infty} -\frac{2r_g L_e N_p k_{pn} k_{dn} \lambda_r^0 F_{m_2}}{np_3}, \quad m_2 p_2 = np_3, \quad n = 1, 2\ldots$$

$$+ \sum_{m_2=1}^{\infty} \sum_{k_2=1}^{\infty} \left[-\frac{r_g L_e N_p k_{pn} k_{dn} \lambda_r^{k_2} F_{m_2}}{np_3} \times \cos(k_2 p_1 \Omega_r t + k_2 p_1 \theta_0) \right], \quad |m_2 p_2 \pm k_2 p_1| = np_3, \quad n = 1, 2\ldots \tag{17}$$

$$\varphi_{\mathrm{PM}}^{R}(t) = \sum_{m_1=1}^{\infty} \left[-\frac{2r_g L_e N_p k_{pn} k_{dn} \lambda_s^0 F_{m_1}}{np_3} \times \cos(m_1 p_1 \Omega_r t + m_1 p_1 \theta_0) \right], \quad m_1 p_1 = np_3, \quad n = 1, 2\ldots$$

$$+ \sum_{m_1=1}^{\infty} \sum_{k_1=1}^{\infty} \left[-\frac{r_g L_e N_p k_{pn} k_{dn} \lambda_s^{k_1} F_{m_1}}{np_3} \times \cos(m_1 p_1 \Omega_r t + m_1 p_1 \theta_0) \right], \quad |m_1 p_1 \pm k_1 p_2| = np_3, \quad n = 1, 2\ldots \tag{18}$$

where $\varphi_{\mathrm{PM}}^{S}(t)$ is the phase PMFL produced by stator PMs; $\varphi_{\mathrm{PM}}^{R}(t)$, indicates the phase PMFL produced by rotor PMs.

From (17) and (18), one can find that to produce PMFL, PPNs of the AFDHs in Table 2 must satisfy the following condition:

$$\{m_1 p_1 \cup |m_1 p_1 \pm k_1 p_2| \cup |m_2 p_2 \pm k_2 p_1|\} = np_3, m_1, m_2, k_1, k_2, n \in N^* \tag{19}$$

Interestingly, if there is an S-I-type harmonic satisfying $m_2 p_2 = np_3$, $\varphi_{\mathrm{PM}}^{S}(t)$ will have a dc bias, thus resulting in a dc bias in $\varphi_{\mathrm{PM}}(t)$. If there are no such AFDHs with $m_2 p_2 = np_3$, $\varphi_{\mathrm{PM}}^{S}(t)$ and $\varphi_{\mathrm{PM}}(t)$ will not have a dc bias. For $\varphi_{\mathrm{PM}}^{R}(t)$, there is absolutely no dc bias.

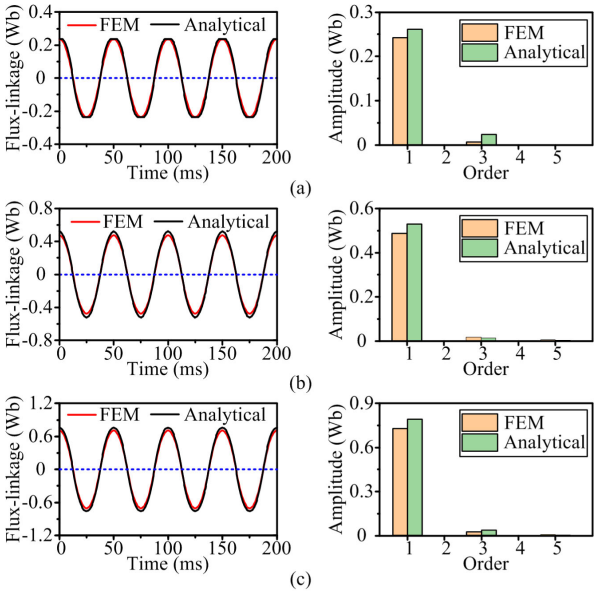

FIGURE 12. PMFL of 12/10 DPME machine. (a) Produced by stator PMs [$\phi_{\mathrm{PM}}^{S}(t)$]. (b) Produced by rotor PMs [$\phi_{\mathrm{PM}}^{R}(t)$]. (c) Produced by both stator and rotor PMs [$\phi_{\mathrm{PM}}(t)$].

To verify the derivation of (15), (17), and (18), PMFLs of the 12/10 DPME machine with linear iron are analyzed by using FEM and the purely analytical method. The analytical and FEM results are presented in Fig. 12. Clearly, the analytical results are basically consistent with the FEM results. Note that although the FEM results for AFD in Fig. 11 (a) and 11 (b) are greater than the analytical results, the FEM

results for PMFL in Figs. 12 (a) and 12 (b) are smaller than the analytical results. The reason is that only AFDHs with specific PPNs can produce PMFL. For example, for the S-I type AFDHs in Fig. 11(c), n is odd for the 12/10 DPME machine due to the full-pitch coils, and the S-I type AFDHs do not satisfy $6m_2 = n$. Thus, although the S-I type AFDHs obtained by FEM are larger than those obtained by the PAMPM, S-I type AFDHs do not produce PMFL. For the S-II- and S-III-type AFDHs in Fig. 11(c), their PPNs satisfy $|m_2p_2 \pm k_2p_1| = np_3$. This means that the S-II and S-III type AFDHs can produce PMFL. However, the AFDHs obtained by FEM are smaller than those obtained by the PAMPM. Moreover, there are no S-I type AFDHs meeting $6m_2 = n$. This means that $\varphi^S_{\rm PM}(t)$ and $\varphi_{\rm PM}(t)$ have no dc bias, which is consistent with the FEM results.

As shown in Fig. 13(a), a 12/8 DPME machine is utilized to verify the case in which S-I type AFDHs satisfying $m_2p_2 = np_3$ will cause the PMFL to have a dc bias. For the 12/8 DPME machine, since $y_1 = 1$, $p_2 = 12$, and $p_3 = 4$, n can be odd according to (16). This means that there are flux density harmonics with $3m_2 = n$. Therefore, $\varphi^S_{\rm PM}(t)$ and $\varphi_{\rm PM}(t)$ have a dc bias, while $\varphi^R_{\rm PM}(t)$ has no dc bias. These are proved by Fig. 13(b). In addition, the dc bias of $\varphi^S_{\rm PM}(t)$ and $\varphi_{\rm PM}(t)$ is about -0.02 Wb.

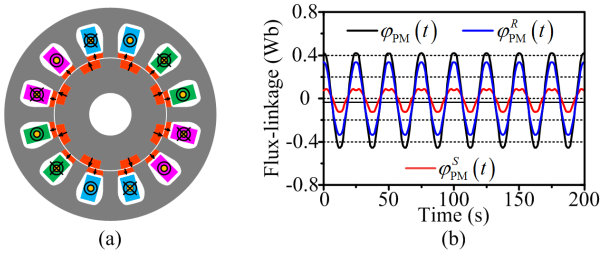

FIGURE 13. 12/8 DPME machine. (a) Configuration. (b) Waveforms of PMFL.

C. BACK-EMF

Phase back-EMF can be obtained based on (15) and Faraday's law of electromagnetic induction. Thus, the phase back-EMF produced by stator PMs, i.e., $E^S_{\rm PM}(t)$, can be calculated by

$$E^S_{\rm PM}(t) = \sum_{m_2=1}^{\infty}\sum_{k_2=1}^{\infty} -\frac{r_g L_e N_p k_{pn} k_{dn} \lambda_r^{k_2} F_{m_2} k_2 p_1 \Omega_r}{np_3} \times \sin(k_2 p_1 \Omega_r t + k_2 p_1 \theta_0), \quad |m_2p_2 \pm k_2p_1| = np_3, \quad n = 1, 2\ldots \tag{20}$$

The phase back-EMF produced by rotor PMs, i.e., $E^R_{\rm PM}(t)$ can be calculated by

$$E^R_{\rm PM}(t) = \sum_{m_1=1}^{\infty} -\frac{2r_g L_e N_p k_{pn} k_{dn} \lambda_s^0 F_{m_1} m_1 p_1 \Omega_r}{np_3} \times \sin(m_1 p_1 \Omega_r t + m_1 p_1 \theta_0), \quad m_1p_1 = np_3, \quad n = 1, 2\ldots$$

TABLE 4. AFDHs that make contribution to the generation of back-EMF.

AFDHs that make a contribution to the generation of $E^S_{\rm PM}(t)$				
AFDHs produced by stator PMs		Corresponding harmonic back-EMF		
Type	Specific PPN	f_v	Angle	E_v
S-I				0
S-II	$m_2p_2 + k_2p_1 = np_3$	$k_2 f$	$k_2 p_1 \theta_0$	$\sum_{m_2=1}^{\infty}\sum_{k_2=1}^{\infty} -\frac{r_g L_e N_p k_{wn} \lambda_r^{k_2} F_{m_2} k_2 p_1 \Omega_r}{np_3}$
S-III	$\lvert m_2p_2 - k_2p_1\rvert = np_3$	$k_2 f$	$k_2 p_1 \theta_0$	$\sum_{m_2=1}^{\infty}\sum_{k_2=1}^{\infty} -\frac{r_g L_e N_p k_{wn} \lambda_r^{k_2} F_{m_2} k_2 p_1 \Omega_r}{np_3}$
AFDHs that make a contribution to the generation of $E^R_{\rm PM}(t)$				
AFDHs produced by rotor PMs		Corresponding harmonic back-EMF		
Type	Specific PPN	f_v	Angle	E_v
R-I	$m_1p_1 = np_3$	$m_1 f$	$m_1 p_1 \theta_0$	$\sum_{m_1=1}^{\infty} -\frac{2r_g L_e N_p k_{wn} \lambda_s^0 F_{m_1} m_1 p_1 \Omega_r}{np_3}$
R-II	$m_1p_1 + k_1p_2 = np_3$	$m_1 f$	$m_1 p_1 \theta_0$	$\sum_{m_1=1}^{\infty}\sum_{k_1=1}^{\infty} -\frac{r_g L_e N_p k_{wn} \lambda_s^{k_1} F_{m_1} m_1 p_1 \Omega_r}{np_3}$
R-III	$\lvert m_1p_1 - k_1p_2\rvert = np_3$	$m_1 f$	$m_1 p_1 \theta_0$	$\sum_{m_1=1}^{\infty}\sum_{k_1=1}^{\infty} -\frac{r_g L_e N_p k_{wn} \lambda_s^{k_1} F_{m_1} m_1 p_1 \Omega_r}{np_3}$

k_{wn} in Table IV refers to the winding factor of *n-th* harmonic. Wherein, $k_{wn} = k_{pn}k_{dn}$.

$$+ \sum_{m_1=1}^{\infty}\sum_{k_1=1}^{\infty} -\frac{r_g L_e N_p k_{wn} \lambda_s^{k_1} F_{m_1} m_1 p_1 \Omega_r}{np_3} \times \sin(m_1 p_1 \Omega_r t + m_1 p_1 \theta_0), \quad |m_1p_1 \pm k_1p_2| = np_3, \quad n = 1, 2\ldots \tag{21}$$

Therefore, the total phase back-EMF produced by stator and rotor PMs, i.e., $E_{\rm PM}(t)$, can be yielded by the sum of $E^S_{\rm PM}(t)$ and $E^R_{\rm PM}(t)$.

From (20) and (21) as well as Table 2, one can find that not all the AFDHs participate in the generation of back-EMF. The AFDHs that generate back-EMF are summarized in Table 4. f in Table 4 refers to the frequency of fundamental back-EMF, where $f = p_1\Omega_r / (2\pi)$. From Table 4, one can find that:

1) Only AFDHs with specific PPNs can produce back-EMF. The PPNs of these specific harmonics are related to p_3 and n. This signifies that the armature windings can select specific AFDHs to generate back-EMF, similar to a filter [36], [37].
2) Five of the six types of AFDHs participate in the generation of back EMF. The five types are S-II, S-III, R-I, R-II, and R-III types. Note that the S-I type AFDHs do not contribute to the generation of back-EMF because these harmonics do not vary with time.
3) Harmonic back-EMFs with the same f_v have the same phase angle, so $E^S_{\rm PM}(t)$ and $E^R_{\rm PM}(t)$ can effectively synthesize $E_{\rm PM}(t)$.
4) The odd- and even-order of back-EMF depends on k_2 and m_1, which meet specific PPNs.

To verify the derivation of (20) and (21), back-EMFs of the 12/10 DPME machine with linear iron are compared by using FEM and the purely analytical method. Fig. 14 shows the analytical and FEM results. As seen from the waveforms,

the analytical results basically correspond with the FEM results. From the three bar charts, one can observe that $E^S_{PM}(t)$, $E^R_{PM}(t)$ and $E_{PM}(t)$ do not contain even-order harmonics. Because n is odd for the 12/10 DPME machine due to the full-pitch coils, k_2 and m_1 cannot satisfy the specific PPNs in Table 4. In contrast, k_2 and m_1 are odd and meet the specific PPNs in Table 4, so $E^S_{PM}(t)$, $E^R_{PM}(t)$ and $E_{PM}(t)$ of the 12/10 DPME machine only have odd-order harmonics.

D. RECOGNIZE AND QUANTIFY THE CONTRIBUTION OF AFDHs TO THE GENERATION OF BACK-EMF

The contribution of AFDHs to the generation of back-EMF can be recognized and quantified according to the PAMPM, as shown in Table 4. It can be observed from Fig. 14 that fundamental back-EMFs are dominant compared with other harmonic back-EMFs. Therefore, we choose to recognize and quantify the contribution of AFDHs to the generation of fundamental back-EMFs. It should be emphasized that the method to analyze the contribution of AFDHs to fundamental back-EMFs is also suitable for the analysis of the contribution of AFDHs to harmonic back-EMFs.

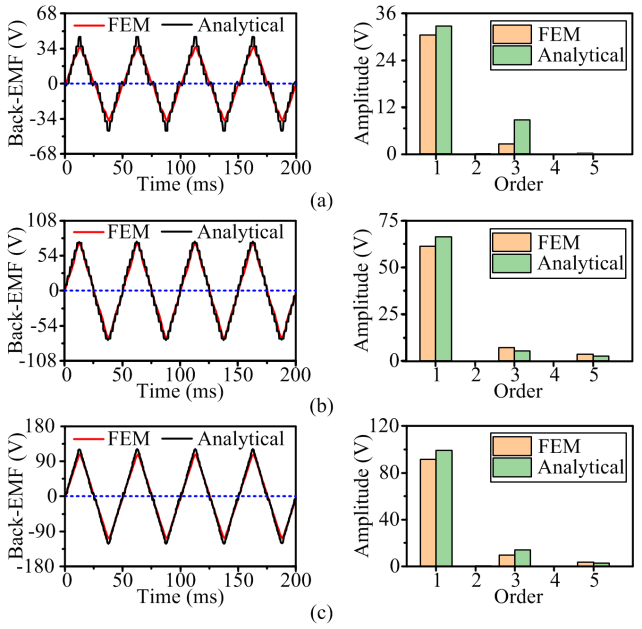

FIGURE 14. Back-EMF and its spectrum. (a) $E^S_{PM}(t)$. (b) $E^R_{PM}(t)$. (c) $E_{PM}(t)$.

By means of the PAMPM, letting $m_1 = k_2 = 1$, the values of m_2 and k_1 range from 1 to 480, and substituting the parameters in Table 1 into Table 4, one can obtain the contribution of the six types of AFDHs to the amplitudes of fundamental back-EMFs. As shown in Table 5, one can see that:

1) Only the S-II, S-III, R-I, R-II, and R-III types of AFDHs contribute to fundamental back-EMFs. S-I type AFDHs do not contribute fundamental back-EMFs.
2) Fundamental back-EMFs produced by the five types of harmonics have the same phase angle, i.e., 4π rad. Therefore, the synthesis of these fundamental back-EMFs is algebraic addition, not vector addition.
3) Not all types of AFDHs make a positive contribution to the amplitude of fundamental back-EMFs. Clearly, the S-II and R-II types of AFDHs make a negative contribution to the generation of fundamental back-EMFs. The amplitudes of fundamental back-EMFs produced by S-II and R-II type AFDHs are negative values, which will cancel out the back-EMFs generated by other AFDHs.

TABLE 5. Contribution of AFDHs to fundamental back-EMFs.

Airgap flux density harmonic		Fundamental back-EMF		
Type	Specific PPN	f_v, Hz	Angle	E_v, V
S-I				V_1=0
S-II	$m_2p_2 + p_1 = np_3, m_2 \in [1,480]$	20	4π	V_2=-2.93
S-III	$\lvert m_2p_2 - p_1\rvert = np_3, m_2 \in [1,480]$	20	4π	V_3=35.82
R-I	$p_1 = np_3$	20	4π	V_4=20.69
R-II	$p_1 + k_1p_2 = np_3, k_1 \in [1,480]$	20	4π	V_5=-4.09
R-III	$\lvert p_1 - k_1p_2\rvert = np_3, k_1 \in [1,480]$	20	4π	V_6=49.95

To evaluate the contribution of AFDHs in Table 5 to the generation of total fundamental back-EMF, the contribution rate (CR) can be defined as

$$\eta_j = V_j / V_t, \quad j = 1, 2, \ldots 6 \tag{22}$$

where η indicates CR; $V_t = V_1 + V_2 + V_3 + V_4 + V_5 + V_6$. For instance, η_2 represents the CR of S-II type AFDHs to total fundamental back-EMF. Fig. 15 gives the CR of the five types of AFDHs. The CRs of S-II and R-II type AFDHs to the total fundamental back-EMF are -2.95% and -4.11%, respectively.

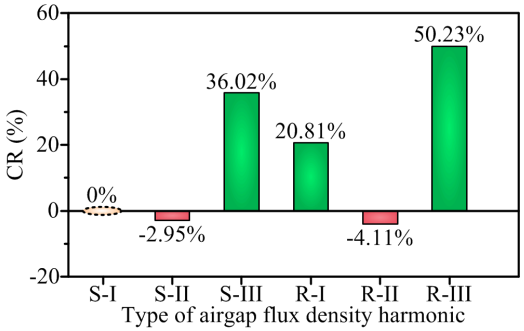

FIGURE 15. CR of six types of AFDHs to total fundamental back-EMF.

Overall, the S-II and R-II types of AFDHs make a negative contribution to the generation of back-EMF. However, which AFDHs in the two types play a negative role in generating back-EMF is still unknown. To solve this problem, one can recognize and quantify AFDHs by virtue of the PAMPM, as shown in Table 4. The recognition and quantification results are listed in Table 6. Note that the larger the PPN is, the smaller the contribution of AFDHs to back-EMF.

TABLE 6. Recognition and quantification of AFDHs in S-II and R-II types.

	Recognize PPN of AFDH		Quantify the contribution of AFDH to back-EMF
Type	(m_2, k_2)	PPN	Amplitude, V
S-II	(1, 1)	22	-3.32
	(3, 1)	46	0.53
	(5, 1)	70	-0.21
	(7, 1)	94	0.11
Type	(m_1, k_1)	PPN	Amplitude, V
R-II	(1,1)	22	-4.6
	(1,3)	46	0.7387
	(1,5)	70	-0.29
	(1,7)	94	0.15

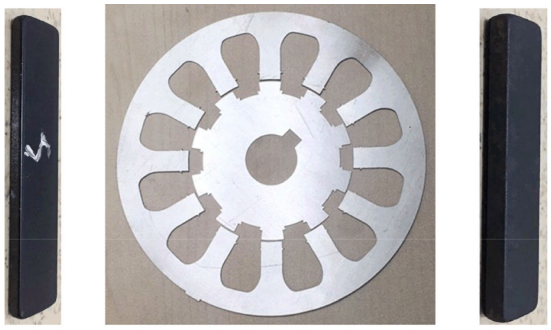

FIGURE 16. Main parts of 12/10 DPME machine. (a) Stator PM. (b) Silicon steel sheet of stator and rotor. (c) Rotor PM.

Therefore, we only recognize and quantify AFDHs with PPNs less than 100. As seen from Table 6, the amplitudes of fundamental back-EMF produced by AFDHs with PPN = 22 and PPN = 70 are negative values, while the amplitude of total fundamental back-EMF (V_t = 99.44 V) and the amplitudes generated by other AFDHs are positive values. Because of the same phase angle, AFDHs with PPN = 22 and PPN = 70 will weaken the back-EMFs generated by other AFDHs. Hence, for S-II and R-II type harmonics, AFDHs with PPN = 22 and PPN = 70 make a negative contribution to the generation of fundamental back-EMF. Apparently, AFDHs with PPN = $p_1 + p_2 = 22$ are the main cause of the negative contribution, which requires special attention at the beginning of EM design.

IV. EXPERIMENTAL TEST

The 3-phase 12/10 DPME machine (see Fig. 1) with nonlinear iron is manufactured on the basis of the parameters in Table 1. The rated power and rated speed of the prototype are 500 W and 120 r/min, respectively. Fig. 16 shows the main parts of the prototype machine. Fig. 17 exhibits the experimental test platform.

To analyze the feasibility of the PAMPM, one can first measure the total phase back-EMF produced by stator and rotor PMs, then obtain the measured amplitude of fundamental back-EMF by FFT, and finally compare the measured amplitude of fundamental back-EMF with the amplitude obtained by the analytical method. Fig. 18 displays the total

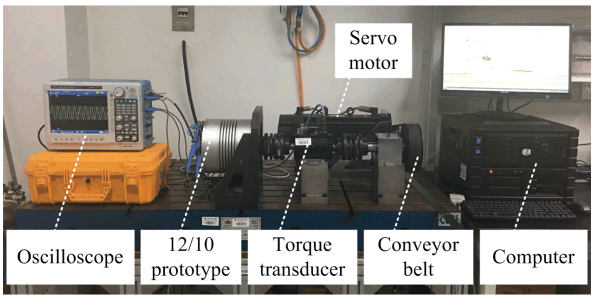

FIGURE 17. Experimental test platform.

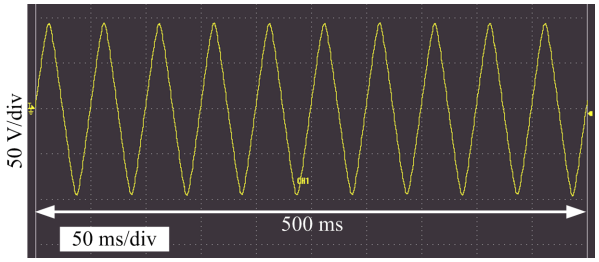

FIGURE 18. Measured total phase back-EMF at 120 r/min.

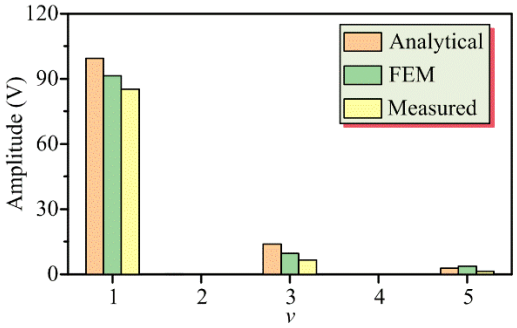

FIGURE 19. Amplitude comparison of harmonic back-EMF at 120 r/min.

phase back-EMF measured by an oscilloscope when the prototype machine operates at 120 r/min. Fig. 19 compares the amplitudes of harmonic back-EMF in three cases.

As shown in Fig. 19, the measured phase back-EMF does not contain any even-order harmonics, which agrees well with the analytical and FEM results. It is undeniable that there are errors in amplitude among the analytical, FEM, and measured results. These errors result from the derivation assumptions of the PAMPM as well as the finite harmonic orders of airgap PM MMF and airgap permeance. Since fundamental back-EMF is dominant among these harmonic back-EMFs, we only analyze the amplitude error of fundamental back-EMF. Comparing the analytical result to the FEM and measured results, the corresponding errors are 8.7% and 16.7%, respectively. Therefore, the PAMPM for the DPME machine is not suitable for high-precision calculation but is useful for EM designers to recognize and quantify AFDHs that make a negative contribution to the generation of back-EMF at the beginning of EM design and then optimize the DPME machine better.

V. CONCLUSION

Herein, a PAMPM for the DPME machine is established to quantitatively analyze the back-EMF. Based on the PAMPM, the general and purely analytical expressions of AFD, PMFL and back-EMF are deduced. The PAMPM and the derived expressions are verified by using 2D FEM. As per the purely analytical expression of back-EMF and the PAMPM, AFDHs that contribute to the generation of back-EMF are recognized and quantified. The feasibility of the PAMPM is analyzed by comparing the total phase back-EMFs obtained by analytical calculation, FEM, and measurement. The main conclusions are summarized as follows:

1) The PAMPM established for DPME machines is a purely analytical method and does not require any numerical method, which is quite simple and intuitive. Especially in the calculation of harmonic coefficients in airgap permeance expression, the PAMPM does not require complicated conformal transformation or solving mathematical equations in different subdomains.
2) According to PPN, AFDHs can be divided into six types. However, five types of AFDHs with specific PPNs participate in the generation of back EMF. It is worth noting that not all five types of AFDHs make a positive contribution to the generation of back EMF. Some will cancel out the back-EMFs generated by other AFDHs.
3) By virtue of the PAMPM, S-II and R-II type AFDHs in the 12/10 DPME machine are recognized as those that make a negative contribution to the generation of back EMF. The CRs of S-II- and R-II-type AFDHs to the total fundamental back-EMF can be quantified and are -2.95% and -4.11%, respectively.
4) It can be recognized by the PAMPM that S-II and R-II type AFDHs with PPN $= 22$ are the main cause of the negative contribution to the generation of back EMF, which needs special attention when designing the 12/10 DPME machine.
5) AFDHs with $m_2p_2 = np_3$ make PM flux-linkage have a dc bias.
6) Comparing the analytical result to the FEM and measured results, the errors are 8.7% and 16.7%, respectively. Therefore, the PAMPM is not suitable for high-precision calculations. However, it is useful for EM designers at the beginning of EM design to recognize and quantify the AFDHs that make a negative contribution to the generation of back-EMF and then optimize the DPME machine better.

APPENDIX

A. DERIVATION OF F_r and F_{r1}

Fig. 20 is used to derive F_r and F_{r1} in (2). In Fig. 20(a), the dotted area represents the model unit (MU). According to the first assumption in Section II and the flux path in Fig. 20(b), the equivalent magnetic circuit (EMC) of the MU can be obtained, as shown in Fig. 20(c). Therefore,

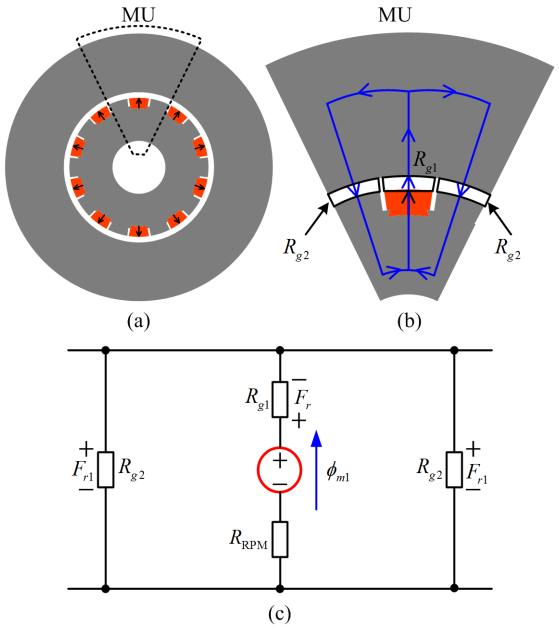

FIGURE 20. Model to calculate F_r and F_{r1}. (a) Model unit. (b) Flux path. (c) Equivalent magnetic circuit of the model unit.

the main flux in Fig. 20(c) can be obtained by

$$\phi_{m1} = F_{\mathrm{RPM}} / \left(R_{\mathrm{RPM}} + R_{g1} + R_{g2}\right) \tag{23}$$

where F_{SPM} is the MMF generated by a rotor PM; R_{SPM} indicates the reluctance of a rotor PM; R_{g1} represents the reluctance of the airgap right above a rotor PM; and R_{g2} stands for the reluctance of the airgap right above a rotor tooth.

The parameters in (23) can be obtained by the following expressions according to the known parameters in Table 1:

$$F_{\mathrm{RPM}} = (B_r h_{rm}) / (\mu_0 u_r) \tag{24}$$

$$R_{g1} = \ln (R_{si}/R_{ro}) / [\mu_0 L_e (K_r \alpha_r - 2\theta_m)] \tag{25}$$

$$R_{g2} = \ln (R_{si}/R_{ro}) / [\mu_0 L_e \alpha_r (1 - K_r)] \tag{26}$$

$$R_{\mathrm{RPM}} = \ln [R_{ro}/ (R_{ro} - h_{rm})] / [\mu_0 u_r L_e (K_r \alpha_r - 2\theta_m)] \tag{27}$$

Thus, F_r and F_{r1} can be calculated by

$$\begin{cases} F_r = \phi_{m1} R_{g1} \\ F_{r1} = \phi_{m1} R_{g2} \end{cases} \tag{28}$$

As seen from (28), if $R_{g1} = R_{g2}$, F_r will be equal to F_{r1}. This means that the waveform of the airgap rotor PM MMF in Fig. 7(a) is symmetrical about the zero of the y-axis. If $R_{g1} \neq R_{g2}$, F_r will be not equal to F_{r1}. This signifies that the waveform of the airgap rotor PM MMF in Fig. 7(a) is unsymmetrical about the zero of the y-axis. For the DPME machine in this paper, due to $K_r = 0.5$ and $\theta_m = 1.45\pi/180$, one can see from (25) and (26) that R_{g1} is not equal to R_{g2}. Based on the parameters in Table 1 and the above expressions, $R_{g1} = 760595\ \mathrm{H}^{-1}$, $R_{g2} = 638055\ \mathrm{H}^{-1}$, $F_r = 441.75$ A, $F_{r1} = 370.58$ A.

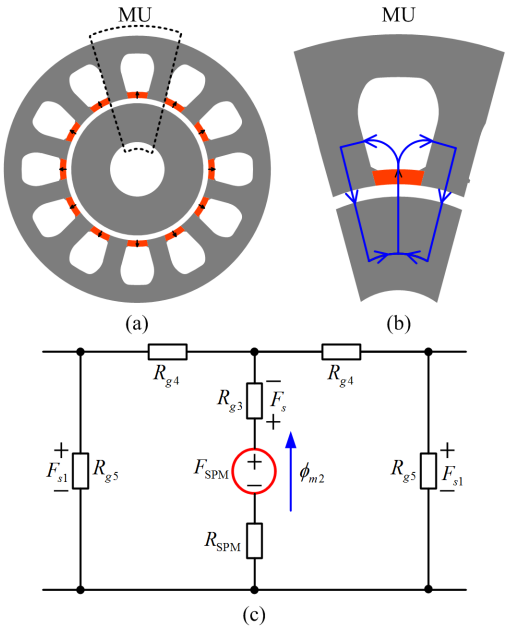

FIGURE 21. Model to calculate F_S and F_{S1}. (a) Model unit. (b) Flux path. (c) Equivalent magnetic circuit of the model unit.

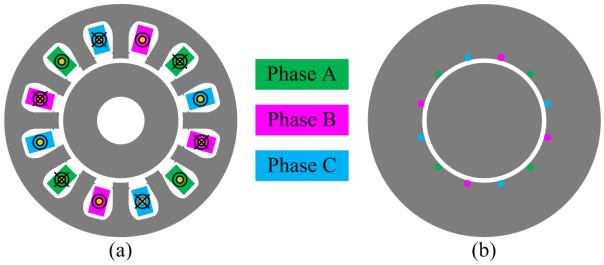

FIGURE 22. FE models to get $\lambda_S(\theta_S)$. (a) FE model to get $B_S(\theta_S)$. (b) FE model to get $F_S(\theta_S)$.

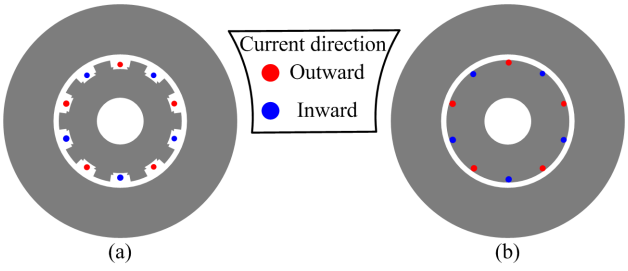

FIGURE 23. FE models to get $\lambda_r(\theta_S)$. (a) FE model to get $B_r(\theta_S)$. (b) FE model to get $F_r(\theta_S)$.

B. DERIVATION OF F_S and F_{S1}

Fig. 21 is used to derive F_s and F_{s1} in (3). In Fig. 21(a), the dotted area represents the MU. According to the first assumption in Section II and the flux path in Fig. 21(b), the EMC of the MU can be obtained, as shown in Fig. 21(c). Therefore, the main flux in Fig. 21(c) can be gotten by

$$\phi_{m2} = F_{\mathrm{SPM}} / \left(R_{\mathrm{SPM}} + R_{g3} + 0.5R_{g4} + R_{g5}\right) \tag{29}$$

where F_{SPM} is the MMF generated by a stator PM; R_{SPM} indicates the reluctance of a stator PM; R_{g3} is the reluctance of the airgap right below a stator PM; R_{g4} represents the reluctance of the flux lines starting from a stator PM and passing through a stator slot, which can be calculated with reference to [47]–[49]; R_{g5} stands for the reluctance of the airgap right below a stator tooth.

One can obtain the parameters in (29) by the following expressions according to the known parameters in Table 1:

$$F_{\mathrm{SPM}} = (B_r h_{sm}) / (\mu_0 u_r) \tag{30}$$

$$R_{g3} = \ln (R_{si}/R_{ro}) / (\mu_0 L_e K_s \alpha_s) \tag{31}$$

$$R_{g4} = \begin{cases} 1 \Big/ \left[\mu_0 L_e \ln \left(\left(h_s + \sqrt{(h_s)^2 + (r_s)^2}\right) \Big/ r_s\right)\right] \\ r_s = 2\left(R_{si} + h_{sm}\right) \sin\left(0.25 K_s \alpha_s\right) \end{cases} \tag{32}$$

$$R_{g5} = \ln (R_{si}/R_{ro}) / [\mu_0 L_e \alpha_s (1 - K_s)] \tag{33}$$

$$R_{\mathrm{SPM}} = \ln [(R_{si} + h_{sm}) / R_{si}] \Big/ (\mu_0 u_r K_s \alpha_s L_e) \tag{34}$$

Thus, F_s and F_{s1} can be calculated by

$$\begin{cases} F_s = \phi_{m2} R_{g3} \\ F_{s1} = \phi_{m2} R_{g5} \end{cases} \tag{35}$$

It can be observed from (35) that when $R_{g3} = R_{g5}$, F_s is the same as F_{s1}, which signifies that the waveform of the airgap stator PM MMF in Fig. 8(a) is symmetrical about the zero of the y-axis. For the DPME machine in this paper, due to $K_s = 0.5$, R_{g3} is equal to R_{g5}. Substituting the parameters in Table 1 into (29)-(35), one can obtain that $R_{g3} = R_{g5} = 765666\ \mathrm{H}^{-1}$, $F_s = F_{s1} = 280.64$ A.

C. FEM TO OBTAIN THE WAVEFORMS OF AIRGAP PERMEANCE

As illustrated in Fig. 22, two finite element (FE) models are built to obtain the waveform of airgap permeance due to the slotted stator in Fig. 9(a). The calculation process contains the following three steps:

Step 1: As shown in Fig. 22(a), 3-phase ac currents are injected into the windings. Due to the field modulation effect (FME) of the slotted stator, the magnetic field generated by ac currents will be modulated by stator teeth. Thus, one can obtain the modulated airgap flux density $[B_s(\theta_s)]$.

Step 2: As shown in Fig. 22(b), the same 3-phase ac currents as Fig. 22(a) are injected into the point windings to obtain the unmodulated MMF $[F_s(\theta_s)]$.

Step 3: As per $\lambda_s(\theta_s) = B_s(\theta_s) / F_s(\theta_s)$, one can obtain the waveform of airgap permeance due to the slotted stator.

Similarly, the two FE models in Fig. 23 are utilized to obtain the waveform of airgap permeance due to the slotted rotor in Fig. 10(a). In Fig. 23(a), dc point currents are distributed in the rotor to obtain the modulated airgap flux density $[B_r(\theta_s)]$. In Fig. 23(b), dc point currents [50] are distributed on the inner surface of the rotor to obtain the unmodulated MMF $[F_r(\theta_s)]$. Therefore, the waveform of airgap permeance due to the slotted rotor can be obtained by the ratio of $B_r(\theta_s)$ to $F_r(\theta_s)$.

REFERENCES

[1] F. Wu and A. M. El-Refaie, "Permanent magnet Vernier machine: A review," *IET Electr. Power Appl.*, vol. 13, no. 2, pp. 127–137, 2019.
[2] H. Zhou, W. Tao, C. Zhou, Y. Mao, G. Li, and G. Liu, "Consequent pole permanent magnet Vernier machine with asymmetric air-gap field distribution," *IEEE Access*, vol. 7, pp. 109340–109348, 2019.
[3] Y. Shi and T. W. Ching, "Power factor analysis of dual-stator permanent magnet Vernier motor with consideration on turn-number assignment of inner and outer stator windings," *IEEE Trans. Magn.*, vol. 57, no. 2, pp. 1–5, Feb. 2021.
[4] A. Arif, N. Baloch, M. Ayub, and B.-I. Kwon, "Wide-speed range operation of PM Vernier machines using wye and wye-delta winding configurations," *IEEE Access*, vol. 8, pp. 194709–194718, 2020.
[5] K. Xie, D. Li, R. Qu, X. Ren, M. R. Shah, and Y. Pan, "A new perspective on the PM Vernier machine mechanism," *IEEE Trans. Ind. Appl.*, vol. 55, no. 2, pp. 1420–1429, Mar. 2019.
[6] Y. Shi and L. Jian, "A novel dual-permanent-magnet-excited machine with flux strengthening effect for low-speed large-torque applications," *Energies*, vol. 11, no. 1, pp. 1–17, Jan. 2018.
[7] L. Xu, W. Zhao, G. Liu, J. Ji, and S. Niu, "A novel dual-permanent-magnet-excited machine with non-uniformly distributed permanent-magnets and flux modulation poles on the stator," *IEEE Trans. Veh. Technol.*, vol. 69, no. 7, pp. 7104–7115, Jul. 2020.
[8] L. Xu, W. Zhao, M. Wu, and J. Ji, "Investigation of slot–pole combination of dual-permanent-magnet-excited Vernier machines by using air-gap field modulation theory," *IEEE Trans. Transport. Electrific.*, vol. 5, no. 4, pp. 1360–1369, Dec. 2019.
[9] Q. Wang, S. Niu, and L. Yang, "Design optimization and comparative study of novel dual-PM excited machines," *IEEE Trans. Ind. Electron.*, vol. 64, no. 12, pp. 9924–9933, Dec. 2017.
[10] S. Jia, R. Qu, W. Kong, D. Li, J. Li, Z. Yu, and H. Fang, "Hybrid excitation stator PM Vernier machines with novel DC-biased sinusoidal armature current," *IEEE Trans. Ind. Appl.*, vol. 54, no. 2, pp. 1339–1348, Mar. 2018.
[11] S. Jia, R. Qu, J. Li, D. Li, and W. Kong, "A stator-PM consequent-pole Vernier machine with hybrid excitation and DC-biased sinusoidal current," *IEEE Trans. Magn.*, vol. 53, no. 6, pp. 1–4, Jun. 2017.
[12] H. Ahmad and J.-S. Ro, "Analysis and design optimization of V-shaped permanent magnet Vernier motor for Torque density improvement," *IEEE Access*, vol. 9, pp. 13542–13552, 2021.
[13] W. Zhao, K. Du, and L. Xu, "Design considerations of fault-tolerant permanent magnet Vernier machine," *IEEE Trans. Ind. Electron.*, vol. 67, no. 9, pp. 7290–7300, Sep. 2020.
[14] Q. Lin, S. Niu, F. Cai, W. Fu, and L. Shang, "Design and optimization of a novel dual-PM machine for electric vehicle applications," *IEEE Trans. Veh. Technol.*, vol. 69, no. 12, pp. 14391–14400, Dec. 2020.
[15] S. Niu, T. Sheng, X. Zhao, and X. Zhang, "Operation principle and torque component quantification of short-pitched flux-bidirectional-modulation machine," *IEEE Access*, vol. 7, pp. 136676–136685, 2019.
[16] L. Jian, Y. Shi, C. Liu, G. Xu, Y. Gong, and C. C. Chan, "A novel dual-permanent-magnet-excited machine for low-speed large-torque applications," *IEEE Trans. Magn.*, vol. 49, no. 5, pp. 2381–2384, May 2013.
[17] W. Zhao, X. Sun, J. Ji, and G. Liu, "Design and analysis of new Vernier permanent-magnet machine with improved torque capability," *IEEE Trans. Appl. Supercond.*, vol. 26, no. 4, pp. 1–5, Jun. 2016.
[18] X. Zhao, S. Niu, and W. Fu, "Torque component quantification and design guideline for dual permanent magnet Vernier machine," *IEEE Trans. Magn.*, vol. 55, no. 6, pp. 1–5, Jun. 2019.
[19] A. Ishizaki, "Theory and optimum design of PM Vernier motor," in *Proc. 7th Int. Conf. Electr. Mach. Drives*, no. 412, Sep. 1995, pp. 208–212.
[20] Y. Gao, M. Doppelbauer, R. Qu, D. Li, and H. Ding, "Synthesis of a flux modulation machine with permanent magnets on both stator and rotor," *IEEE Trans. Ind. Appl.*, vol. 57, no. 1, pp. 294–305, Jan./Feb. 2021.
[21] D. Cao, W. Zhao, J. Ji, L. Ding, and J. Zheng, "A generalized equivalent magnetic network modeling method for vehicular dual-permanent-magnet Vernier machines," *IEEE Trans. Energy Convers.*, vol. 34, no. 4, pp. 1950–1962, Dec. 2019.
[22] K. Xie, D. Li, R. Qu, and Y. Gao, "A novel permanent magnet Vernier machine with Halbach array magnets in stator slot opening," *IEEE Trans. Magn.*, vol. 53, no. 6, pp. 1–5, Jun. 2017.
[23] D. K. Jang and J. H. Chang, "Design of a Vernier machine with PM on both sides of rotor and stator," *IEEE Trans. Magn.*, vol. 50, no. 2, pp. 877–880, Feb. 2014.
[24] Q. Wang and S. Niu, "A novel hybrid-excited dual-PM machine with bidirectional flux modulation," *IEEE Trans. Energy Convers.*, vol. 32, no. 2, pp. 424–435, Jun. 2017.
[25] Q. Wang and S. Niu, "Design, modeling, and control of a novel hybrid-excited flux-bidirectional-modulated generator-based wind power generation system," *IEEE Trans. Power Electron.*, vol. 33, no. 4, pp. 3086–3096, Apr. 2018.
[26] Q. Wang, S. Niu, and X. Luo, "A novel hybrid dual-PM machine excited by AC with DC bias for electric vehicle propulsion," *IEEE Trans. Ind. Electron.*, vol. 64, no. 9, pp. 6908–6919, Sep. 2017.
[27] L. Jian, Y. Shi, J. Wei, Y. Zheng, and Z. Deng, "Design optimization and analysis of a dual-permanent-magnet-excited machine using response surface methodology," *Energies*, vol. 8, no. 9, pp. 10127–10140, Sep. 2015.
[28] Y. Shi, S. Niu, J. Wei, L. Jian, and R. Liu, "Comparison between dual-permanent-magnet-excited machines with fewer stator poles and fewer rotor poles," *IEEE Trans. Magn.*, vol. 51, no. 3, pp. 1–4, Mar. 2015.
[29] S. Niu, S. L. Ho, and W. N. Fu, "A novel stator and rotor dual PM Vernier motor with space vector pulse width modulation," *IEEE Trans. Magn.*, vol. 50, no. 2, pp. 805–808, Feb. 2014.
[30] S. Wang, S. Niu, and W. Fu, "Comparative study of relieving-DC-saturation hybrid excited Vernier machine with different rotor pole designs for wind power generation," *IEEE Access*, vol. 8, pp. 198900–198911, 2020.
[31] J. Huang, W. Fu, S. Niu, and X. Zhao, "Comparative analysis of different permanent magnet arrangements in a novel flux modulated electric machine," *IEEE Access*, vol. 9, pp. 14437–14445, 2021.
[32] X. Ren, D. Li, R. Qu, and T. Pei, "Back EMF harmonic analysis of permanent magnet magnetic geared machine," *IEEE Trans. Ind. Electron.*, vol. 67, no. 8, pp. 6248–6258, Aug. 2020.
[33] B. Gaussens, E. Hoang, O. de la Barriere, J. Saint-Michel, M. Lecrivain, and M. Gabsi, "Analytical approach for air-gap modeling of field-excited flux-switching machine: No-load operation," *IEEE Trans. Magn.*, vol. 48, no. 9, pp. 2505–2517, Sep. 2012.
[34] S. Jia, R. Qu, J. Li, and D. Li, "Principles of stator DC winding excited Vernier reluctance machines," *IEEE Trans. Energy Convers.*, vol. 31, no. 3, pp. 935–946, Sep. 2016.
[35] H. Wen and M. Cheng, "Unified analysis of induction machine and synchronous machine based on the general airgap field modulation theory," *IEEE Trans. Ind. Electron.*, vol. 66, no. 12, pp. 9205–9216, Dec. 2019.
[36] X. Zhu, W. Hua, W. Wang, and W. Huang, "Analysis of back-EMF in flux-reversal permanent magnet machines by air gap field modulation theory," *IEEE Trans. Ind. Electron.*, vol. 66, no. 5, pp. 3344–3355, May 2019.
[37] M. Cheng, H. Wen, P. Han, and X. Zhu, "Analysis of airgap field modulation principle of simple salient poles," *IEEE Trans. Ind. Electron.*, vol. 66, no. 4, pp. 2628–2638, Apr. 2019.
[38] Y. Zhang, J. Zhang, and R. Liu, "Magnetic field analytical model for magnetic harmonic gears using the fractional linear transformation method," *Chin. J. Electr. Eng.*, vol. 5, no. 1, pp. 47–52, Mar. 2019.
[39] S. Hyoseok, N. Niguchi, and K. Hirata, "Characteristic analysis of surface permanent-magnet Vernier motor according to pole ratio and winding pole number," *IEEE Trans. Magn.*, vol. 53, no. 11, pp. 1–4, Nov. 2017.
[40] Y. Oner, Z. Q. Zhu, L. J. Wu, X. Ge, H. Zhan, and J. T. Chen, "Analytical on-load subdomain field model of permanent-magnet Vernier machines," *IEEE Trans. Ind. Electron.*, vol. 63, no. 7, pp. 4105–4117, Jul. 2016.
[41] Z. Q. Zhu, L. J. Wu, and Z. P. Xia, "An accurate subdomain model for magnetic field computation in slotted surface-mounted permanent-magnet machines," *IEEE Trans. Magn.*, vol. 46, no. 4, pp. 1100–1115, Apr. 2010.
[42] Y. Yang, G. Liu, X. Yang, and X. Wang, "Analytical electromagnetic performance calculation of Vernier hybrid permanent magnet machine," *IEEE Trans. Magn.*, vol. 54, no. 6, pp. 1–12, Jun. 2018.
[43] B. Gaussens, E. Hoang, O. de la Barriere, J. Saint-Michel, P. Manfe, M. Lecrivain, and M. Gabsi, "Analytical armature reaction field prediction in field-excited flux-switching machines using an exact relative permeance function," *IEEE Trans. Magn.*, vol. 49, no. 1, pp. 628–641, Jan. 2013.
[44] L. Jian, K. T. Chau, Y. Gong, C. Yu, and W. Li, "Analytical calculation of magnetic field in surface-inset permanent magnet motors," *IEEE Trans. Magn.*, vol. 45, no. 10, pp. 4688–4691, Oct. 2009.
[45] J. Hu, F. Liu, and Y. Li, "An improved sub-domain model of flux switching permanent magnet machines considering harmonic analysis and slot shape," *IEEE Access*, vol. 9, pp. 55260–55270, 2021.
[46] J. Yang, C. Ye, S. Huang, Y. Li, F. Xiong, Y. Zhou, and W. Xu, "Analysis of the electromagnetic performance of homopolar inductor machine through nonlinear magnetic equivalent circuit and air-gap permeance function," *IEEE Trans. Ind. Appl.*, vol. 56, no. 1, pp. 267–276, Jan. 2020.

[47] S. Jiang, G. Liu, W. Zhao, L. Xu, and Q. Chen, "Modeling and analysis of spoke-type permanent magnet Vernier machine based on equivalent magnetic network method," *Chin. J. Electr. Eng.*, vol. 4, no. 2, pp. 96–103, Jun. 2018.
[48] G. Liu, L. Ding, W. Zhao, Q. Chen, and S. Jiang, "Nonlinear equivalent magnetic network of a linear permanent magnet Vernier machine with end effect consideration," *IEEE Trans. Magn.*, vol. 54, no. 1, pp. 1–9, Jan. 2018.
[49] Z. Zhu, H. Zhu, X. Li, J. Zhu, and M. Cheng, "Dynamic equivalent magnetic network analysis of an axial PM bearingless flywheel machine," *IEEE Access*, vol. 9, pp. 32425–32435, 2021.
[50] L. R. Huang, J. H. Feng, S. Y. Guo, J. X. Shi, W. Q. Chu, and Z. Q. Zhu, "Analysis of torque production in variable flux reluctance machines," *IEEE Trans. Energy Convers.*, vol. 32, no. 4, pp. 1297–1308, Dec. 2017.

YUJUN SHI (Member, IEEE) was born in Hubei, China, in 1986. He received the M.Sc. degree from Jiangsu University, Zhenjiang, China, in 2013. He is currently pursuing the Ph.D. degree with the Department of Electromechanical Engineering, University of Macau, Macao, China.

From 2013 to 2014, he was a Research Assistant with the Shenzhen Institutes of Advanced Technology, Chinese Academy of Sciences, Shenzhen, China. From 2015 to 2018, he was an Assistant Research Fellow with the Department of Electrical and Electronic Engineering, Southern University of Science and Technology, Shenzhen. His research interests include the design, analysis, and optimization of permanent-magnet electric machines.

JUNWEN ZHONG received the B.S. and Ph.D. degrees from the Huazhong University of Science and Technology, China, in 2011 and 2016, respectively.

From 2016 to 2019, he was a Postdoctoral Researcher with the University of California at Berkeley, Berkeley, CA, USA. From 2019 to 2020, he was a Special Postdoctoral Researcher with RIKEN, Japan. He is currently an Assistant Professor with the Department of Electromechanical Engineering, University of Macau. His research interests include mechanical actuators, soft robots, flexible sensors, and self-powered systems.

LINNI JIAN (Senior Member, IEEE) was born in Hubei, China, in 1983. He received the B.Eng. degree from the Huazhong University of Science and Technology, Wuhan, China, in 2003, the M.Eng. degree from the Institute of Electrical Engineering, Chinese Academy of Sciences, Beijing, China, in 2006, and the Ph.D. degree from The University of Hong Kong, Hong Kong, in 2010.

He is currently an Associate Professor with the Department of Electrical and Electronic Engineering, Southern University of Science and Technology, Shenzhen, China. He also works as the Director of the Shenzhen Key Laboratory of Electric Direct Drive Technology. He is also the holder of more than 30 patents. His research interests include electrical machines and electric drives, power electronics, wireless charging technology for EVs, vehicle-to-grid technology, and smart microgrids. In these areas, he has published more than 80 refereed technical articles, two monographs, and several book chapters.